

www.acsami.org Research Article

# Tribochemistry of Diamond-like Carbon: Interplay between Hydrogen Content in the Film and Oxidative Gas in the Environment

Seokhoon Jang, Muztoba Rabbani, Andrew L. Ogrinc, Maxwell T. Wetherington, Ashlie Martini, and Seong H. Kim\*



Cite This: https://doi.org/10.1021/acsami.3c05316



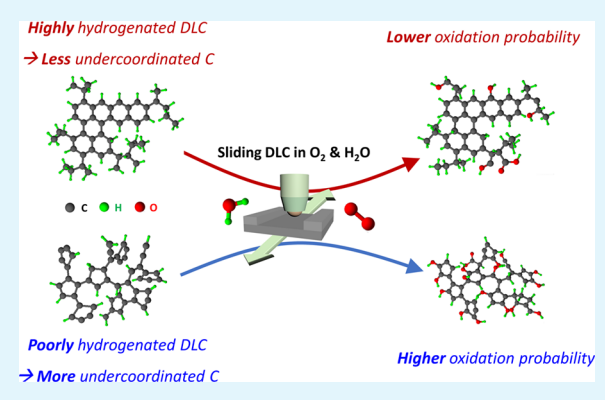
**ACCESS** I

III Metrics & More

Article Recommendations

sı Supporting Information

ABSTRACT: The lubricity of hydrogenated diamond-like carbon (HDLC) films is highly sensitive to the hydrogen (H) content in the film and the oxidizing gas in the environment. The tribochemical knowledge of HDLC films with two different H-contents (mildly hydrogenated vs highly hydrogenated) was deduced from the analysis of the transfer layers formed on the counter-surface during friction tests in  $O_2$  and  $H_2O$  using Raman spectroscopic imaging and X-ray photoelectron spectroscopy (XPS). The results showed that, regardless of H-content in the film, shear-induced graphitization and oxidation take place readily. By analyzing the  $O_2$  and  $H_2O$  partial pressure dependence of friction of HDLC with a Langmuir-type reaction kinetics model, the oxidation probability of the HDLC surface exposed by friction as well as the removal probability of the oxidized species by friction were determined. The HDLC film with more H-content exhibited a lower



oxidation probability than the film with less H-content. The atomistic origin of this H-content dependence was investigated using reactive molecular dynamics simulations, which showed that the fraction of undercoordinated carbon species decreased as the H-content in the film increased, corroborating the lower oxidation probability of the highly-hydrogenated film. The H-content in the HDLC film influenced the probabilities of oxidation and material removal, both of which vary with the environmental condition.

KEYWORDS: hydrogenated diamond-like carbon, superlubricity, surface oxidation, environmental sensitivity, shear-induced graphitization

#### 1. INTRODUCTION

Diamond-like carbon (DLC) has superior mechanical properties<sup>1</sup> and wear protection,<sup>2</sup> which makes it attractive for solid lubrication in engineering systems such as extreme ultraviolet lithography instruments, 3,4 mechanical shaft seals, 5,6 bearings, etc. The C-C connectivity in DLC changes with its chemical composition, <sup>8,9</sup> which is, in turn, very sensitive to deposition temperature <sup>10</sup> and precursor gases used during synthesis. 1,11-13 For example, when DLC is produced via a plasmaenhanced chemical vapor deposition (PECVD) using a precursor gas of C<sub>2</sub>H<sub>2</sub>, the DLC contains ~30 at.% of hydrogen (H); this "mildly hydrogenated" DLC was previously called NFC-10, 11 but will be called 30-HDLC in this study. 1 When DLC is produced via the same PECVD process with a mixture of 25% CH<sub>4</sub> and 75% H<sub>2</sub>, the DLC contains ~40 at.% of H; this "highly hydrogenated" DLC was previously called NFC-6,<sup>11</sup> but will be called 40-HDLC here.<sup>14</sup> The 40-HDLC has a larger graphitic sp<sup>2</sup>-C domain size than the 30-HDLC. 14

The friction behavior of these HDLC coatings varies drastically depending on the environmental condition in which friction is tested. In vacuum 16,17 or dry  $N_2$ , 18–20 the coefficient of friction (COF,  $\mu$ ) of 40-HDLC usually starts high (~0.25) and, after a transient or run-in period, decreases

to a superlubricious value ( $\mu \leq 0.01$ ). On the contrary, 30-HDLC has a higher COF (>0.7) after the run-in period in the same vacuum or inert conditions. <sup>2,12,14,21,22</sup> In ambient air conditions, however, the COFs of both 30- and 40-HDLC converge to around 0.1–0.2. <sup>17,23,24</sup> This environment dependence has been attributed to defect sites at the HDLC surface exposed by sliding, which react with molecules impinging from the gas environment. <sup>17,19,20,23–26</sup>

Although the environmental sensitivity of HDLC surfaces with different H-contents and sp<sup>2</sup>-graphitic domains has been well documented, its molecular origins are not well understood. This lack of understanding is associated with the unstable nature of defect sites exposed by friction. The wear tracks formed on HDLC in an inert atmosphere such as dry  $N_2$  are readily oxidized even with a brief exposure to ambient air;  $^{27-30}$  this makes it extremely difficult to move the sample,

Received: April 13, 2023 Accepted: June 1, 2023



without altering its surface chemistry, from the environment-controlled tribo-testing system to X-ray photoelectron spectroscopy (XPS) or X-ray absorption spectroscopy (XAS) systems. Thus, ex situ chemical analyses of wear tracks formed in an inert atmosphere are affected by the contribution from the air-oxidized surface layer formed while moving the sample. Similarly, HDLC surfaces tested in a controlled environment can be oxidized further upon exposure to air. The thickness of the air-oxidized layer is self-limiting to 1–2 nm due to the transport limit of oxidants in air ( $O_2$  and  $H_2O$ ) into the amorphous carbon network at room temperature. <sup>27–29,31</sup> This is much thinner than the probe depth of XPS and XAS, <sup>15,24</sup> but it still affects the analysis.

To investigate the origin of superlubricity of HDLC without complications due to air-oxidation, in situ transmission electron microscopy (TEM)<sup>32,33</sup> and in situ Raman spectroscopy<sup>18,34,35</sup> have been employed and these approaches indeed were able to find shear-induced evolution of the DLC into more sp<sup>2</sup>-graphitic structures. However, they still cannot provide critical insights relevant to the environmental sensitivity of HDLC films. TEM needs to be operated in high vacuum conditions and probes only small regions at a limited number of locations;<sup>36</sup> thus, it is often difficult to evaluate statistical significance across the entire sliding contact region of amorphous carbon materials which are inherently inhomogeneous. 14,37 In the case of in situ Raman analysis, the probe depth is so deep (for example, >500 nm if the excitation laser wavelength is 532 nm) that its analysis of the wear track is affected by the contribution of the bulk HDLC film.<sup>14</sup>

One possible way of avoiding such complications is ex situ analysis of the transfer layer that remains on the countersurface after tribo-testing of HDLC in controlled environments. Since the tribological interface is not in equilibrium, its chemistry and structure will inherently have a path or history dependence. Thus, the *post-mortem* analysis of the transfer layer could provide critical insights into the chemistry and structure of the shear plane during the friction test, which cannot be obtained (or are difficult to obtain) otherwise. Transfer layers formed on counter-surfaces have been found to be 100-200 nm-thick; 14,18 thus, they can be analyzed with Raman spectroscopy if the counter-surface does not have any Raman signals in the spectral region of the transfer layers. Indeed, this approach of employing ex situ Raman analysis of the transfer layer was able to identify differences in the Hcontent and degree of shear-induced graphitization that could be related to the friction behavior of 30- and 40-HDLC in inert  $(N_2)$  and reducing  $(H_2)$  conditions.<sup>14</sup>

In this study, we used the same ex situ Raman analysis approach in an attempt to understand the sensitivity of friction of 30- and 40-HDLC to the presence of O<sub>2</sub> and H<sub>2</sub>O in the tribo-testing environment. We also evaluated if the ex situ XPS analysis of the transfer layer could provide additional insights into the chemical composition of the transfer layer oxidized during the friction test in O2 and H2O environments. These ex situ analyses of transfer layers were then complemented by analysis of the O2 and H2O partial pressure dependence of HDLC friction with a Langmuir-type reaction kinetics model, corroborated by reactive molecular dynamics (MD) simulations. Combining all these results, a more comprehensive model was proposed to describe the dynamic and reactive processes occurring at the tribological interface of HDLC under the impingement of oxidizing agents in ambient air (O2 and  $H_2O$ ).

#### 2. EXPERIMENTAL DETAILS

**2.1. Preparation of HDLC Films.** Both 40-HDLC and 30-HDLC substrates were produced on Si(100) wafers via the PECVD process, which was described fully elsewhere.  $^{11,13}$  In short, after the Si substrate was sputtered in an argon plasma, a bonding layer of  $\sim\!100$  nm-thick silicon was deposited. The substrate was exposed to a reactive plasma produced from a mixture of 25% CH<sub>4</sub> and 75% H<sub>2</sub> to create  $\sim\!1~\mu$ m-thick 40-HDLC. Similarly, 30-HDLC was fabricated using the same procedure with plasma of 100% C<sub>2</sub>H<sub>2</sub> and had similar thickness. The endogenous hydrogen content of the 40- and 30-HDLC films (40 and 30 at.%) was determined by the hydrogen forward scattering (HFS) method, as reported previously.  $^{38}$ 

2.2. Bidirectional Ball-on-Flat Tribo-Testing. The COF was measured with a custom-built ball-on-flat bidirectional-reciprocating tribometer.<sup>39–41</sup> All friction tests were repeated at least three times to confirm reproducibility (Figures S4 and S5). Before the friction tests, the HDLC surfaces were rinsed with ethanol, and then with deionized water, followed by blow-drying with nitrogen gas to remove any contaminants. 42 The HDLC sample was mounted in a continuous gas flow cell, and an AISI 440C bearing-grade stainless-steel (SS) ball with a diameter of 3 mm and a root-mean-square (RMS) surface roughness of ~10 nm was placed on top of the HDLC substrate as the counter body with an applied load of 2 N. 43 The reciprocating motion was conducted at a sliding speed of 3 mm/s over a span of 2.5 mm. At this sliding speed and normal load, the temperature rise produced by frictional sliding at the HDLC surfaces was estimated to be only ~3 K, 25 which implies that the effect of frictional heat on the sliding interface is negligible in this study.

The extended Hertzian contact mechanics theory, <sup>44</sup> that accounts for the effects of both the Si substrate and HDLC coating, was used to estimate contact area and maximum contact pressure. On the 40-HDLC film which had an elastic modulus of 55 GPa, <sup>1,43</sup> the contact area ( $A_{\rm Hertz}$ ) and the maximum contact pressure ( $P_{\rm Contact}$ ) were estimated to be 2920  $\mu$ m² and 1.06 GPa, respectively. The 30-HDLC had an elastic modulus of 200 GPa, <sup>1</sup> the same theory estimated the contact area  $A_{\rm Hertz} = 2750~\mu$ m² and the maximum contact pressure  $P_{\rm Contact} = 1.08$  GPa. The hardness of 40- and 30-HDLC was reported to be 8 and 27 GPa, respectively. <sup>1,43</sup>

An ultrahigh purity  $N_2$  gas (purity >99.994%; based on the supplier's specification) was flown continuously into the environmental cell during the friction test as a background gas carrying oxidizing gases. The dry oxygen gas environment was prepared by mixing the nitrogen gas stream with an ultrahigh purity oxygen gas (UHP-grade, purity >99.994%; based on the supplier's specification) at a pre-determined ratio for a desired partial pressure of oxygen. The relative humidity (RH) was controlled by mixing the same nitrogen gas with a saturated stream of water vapor at a pre-determined ratio. <sup>45</sup> All experiments were carried out at ambient pressure and room temperature.

2.3. Raman Analyses of Pristine HDLC and Transfer Layers on SS. Raman analysis of pristine HDLC and transfer layers was performed using a Horiba LabRam system with a 100× objective lens (NA = 0.95). The Raman spectrometer was calibrated based on the Si line at 520 cm<sup>-1</sup>. Neutral density filters were utilized to minimize carbon sample burning and the data acquisition time was 5 s with a laser power of 1 mW. At this condition, the estimated power density was  $\sim 2.7 \times 10^5 \text{ W/cm}^2$  and no beam damage of HDLC was noticed. A monochromatic 532 nm laser was chosen to empirically estimate the H content, elastic modulus, and density of HDLC and transfer layers. 46 For the empirical quantification of the sp3-C content of pristine HDLC and transfer layers, 47-50 Raman spectra were measured at multiple wavelengths (229, 364, 488, 532, and 633 nm) (see Figures S2 and S3). A 300 gr/mm grating was used for 532 and 633 nm lasers, and a 600 gr/mm grating was used for 229, 364, and 488 nm lasers.

**2.4.** XPS Analyses of Pristine HDLC and Transfer Layers on **55.** XPS analysis of pristine HDLC and transfer layers was carried out using a PHI VersaProbe III spectrometer to probe the oxidation state, especially the O/C ratio, of these samples. The X-ray source was a monochromatic Al  $K\alpha$  source. The transfer layer sample was exposed

to ambient air for at least 10 min during the sample transfer from the environment-controlled tribo-testing system to the XPS chamber. To compensate for sample charging, the peak position of the saturated C 1s peak was adjusted to 285 eV. High-resolution XPS spectra of C 1s and O 1s were obtained at a pass energy of 69 eV. The atomic concentrations of carbon and oxygen were estimated from the peak area measured in the high-resolution spectra after correcting with the relative sensitivity factors determined for our spectrometer using standard samples. The C 1s peaks were fitted with the CASA software into four components, 285.0, 286.4, 287.6, and 289.0 eV, with the same line shape and width. The background was removed by the Shirley method.

**2.5.** Contact Angles of Water and Diiodomethane (DIM) on 30- and 40-HDLC Films. The measurement of contact angles of water and DIM on 30- and 40-HDLC films was based on the sessile drop method. The contact angles were measured using a ramé-hart Model 295 automated goniometer/tensiometer. After a single drop of liquid on 30- and 40-HDLC films, the contact angle was measured 10 times for 1 s and then averaged. Fowkes theory was utilized to calculate surface energy. <sup>51</sup>

2.6. Computational Methods. Large-scale Atomic/Molecular Massively Parallel Simulator (LAMMPS) and OVITO were used for reactive molecular dynamics (MD) simulations and visualizations. 52,53 The interatomic interactions were modeled using a ReaxFF force field that was capable of reproducing physical properties of various carbon allomorphs and previously used to study the wear and tribochemical reactions of carbon materials in H<sub>2</sub> gas.<sup>54</sup> In MD, an amorphous carbon (a-C) structure was produced by rapidly quenching a high temperature carbon structure in four steps. The first three steps were performed in the microcanonical ensemble (NVT) using the Nosé-Hoover thermostat with a damping parameter of 20 fs. First, initial structures were heated from room temperature to 8000 K at a heating rate of 1000 K/ps. Second, the model was equilibrated at 8000 K for 10 ps. Third, the temperature was decreased to 300 K at a rate of 770 K/ps. Finally, the amorphous structures were relaxed at constant pressure and temperature (NPT) using the Nosé-Hoover thermostat and barostat with damping parameters of 20 and 200 fs, respectively, for 40 ps until the potential energy reached a steady state. The dimensions of a-C after this process were approximately  $1.9 \times 3.15 \times$ 4.5 nm<sup>3</sup>. It should be noted that the surface of the model a-C may not be the same as the HDLC surface in the friction tests due to the nonequilibrium nature of this material system. Nonetheless, the general trend of chemical reactivity of a-C surfaces with different Hcontents is expected to provide insights relevant to the HDLC experiments.

Four a-C structures were constructed with homogeneous concentrations of hydrogen of 10, 20, 30, and 40 at.%; they will be called a-C:10-H, a-C:20-H, a-C:30-H, and a-C:40-H. The height of the simulations cells was extended to create a-C surfaces such that the model systems were  $4.2 \times 3.15 \times 4.5 \text{ nm}^3$ , followed by the thermal equilibration in the NVT ensemble again. To model the oxidation of a-C:H with water and oxygen, either 150 water molecules or 286 oxygen molecules were placed above the a-C:H films (see Figure S1). The boundaries of the model systems in the surface-normal direction were defined by fixing the positions of the bottom most 0.3 nm of a-C:H and adding a reflective wall at the top of the model system. Periodic boundary conditions were applied in the directions in the plane of the surface. The reaction of a-C:H with water or oxygen molecules was allowed by running the simulation in the NVT ensemble at room temperature. The formation of C-O bonds between C in a-C:H and O in water or oxygen was tracked during the simulations for 200 ps, after which no new bonds were observed to form.

# 3. RESULTS AND DISCUSSION

**3.1.** Chemical Properties of Bulk HDLC and Its Top Surface. The pristine 30- and 40-HDLC films (before friction testing) were analyzed with Raman spectroscopy (probing several hundred nm's) and XPS (probing top ~10 nm). In the

Raman spectra, shown in Figure 1a,b, there are two characteristic bands, a D band at ~1350 cm<sup>-1</sup> and a G band

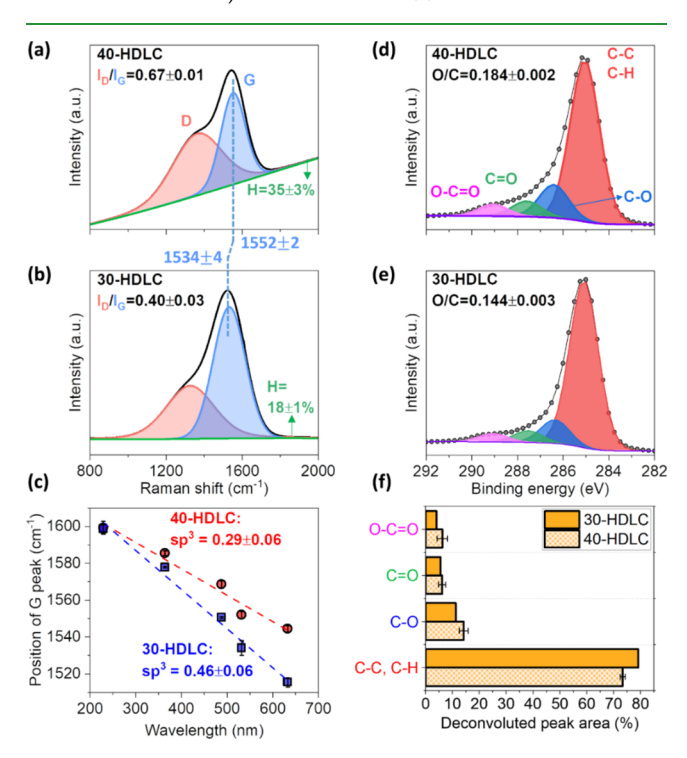


**Figure 1.** Deconvoluted Raman spectra collected from pristine surfaces of (a) 40-HDLC and (b) 30-HDLC (data collected in our previous study <sup>14</sup>). (c) Position of the Raman G band as a function of wavelength of excitation laser for empirical estimation of sp<sup>3</sup>-C content inside pristine HDLCs. Raman spectra collected with different excitation wavelengths (229, 364, 488, 532, and 633 nm) are shown in Figure S2 in the Supporting Information. Deconvoluted high-resolution C 1s XPS spectra of (d) 40-HDLC and (e) 30-HDLC along with its O/C ratio in the inset and (f) deconvoluted peak area of C-bonds.

at ~1580 cm<sup>-1</sup>, arising from the breathing modes of sp<sup>2</sup> graphitic carbon in ring structures and the stretching modes of sp<sup>2</sup> or sp<sup>3</sup> carbons in chain and ring structures, respectively.  $^{46,55}$  The intensity ratio of these two bands  $(I_{\rm D}/I_{\rm G})$  was related to the size of graphitic sp<sup>2</sup>-C domain in films.  $^{46,55}$  Furthermore, the sp<sup>3</sup>-C content (Figure 1c) was quantified from the dispersion of the G band position (see Figure S2) using an empirical correlation.  $^{14,47-50}$  The H-content of the film was calculated from the fluorescence background in this spectral region, and the density and modulus were approximated from the G-band width using empirical equations.  $^{14,56-59}$  All these properties, summarized in Table 1, indicated that 40-HDLC has a larger graphitic domain size, more sp<sup>2</sup>-C content, and higher H-content than 30-HDLC.

The XPS analysis showed a slightly more oxygen content in the 40-HDLC surface (Figure 1d) than the 30-HDLC surface (Figure 1e). The deconvoluted C 1s XPS signal showed that the fraction of C-O and O-C=O species was higher in the air-oxidized surface of 40-HDLC than that of 30-HDLC (Figure 1f). The thickness of the air-oxidized layer was previously estimated to be 1-2 nm. <sup>27-29</sup> The polar component of surface energy calculated from contact angle measurements (see Table 1 and Figure S2c) was larger for the 40-HDLC than the 30-HDLC surface, which appeared to correlate with the

Table 1. Structural Properties of Pristine 40- and 30-HDLC Films Determined from Raman Analysis, 56,57 Chemical

Composition from XPS, and Surface Energy from Contact Angle Measurement (See Figure S2c)<sup>a</sup>

		40-HDLC	30-HDLC
Raman band parameters	$I_{ m D}/I_{ m G}$	$0.67 \pm 0.01$	$0.40 \pm 0.03$
	$G_{\mathrm{Pos}} \left[ \mathrm{cm}^{-1} \right]$	$1552 \pm 2$	$1534 \pm 4$
	$G_{\mathrm{FWHM}}$ [cm <sup>-1</sup> ]	$153 \pm 1$	$199 \pm 4$
physical properties calculated by processing Raman spectral features with empirical equations	fraction of $sp^3 C (sp^2 - C)$	$0.29 \pm 0.06 (0.72 \pm 0.06^{\dagger})$	$0.46 \pm 0.06 \ (0.51^{\ddagger})$
	H content [at. %]	$35 \pm 3 \; (\sim 40^{\$})$	$18 \pm 1 \; (\sim 30^{\$})$
	elastic modulus [GPa]	$200 \pm 2 \ (\sim 60^{\parallel})$	$415 \pm 20 \ (\sim 200^{\parallel})$
	density [g/cm <sup>3</sup> ]	$1.94 \pm 0.01$	$2.44 \pm 0.05$
atomic concentration determined from XPS C 1s and O 1s spectra	C [at. %]	$84.5 \pm 0.1$	$87.4 \pm 0.2$
	O [at. %]	$15.5 \pm 0.1$	$12.6 \pm 0.2$
surface energy [mN/m] obtained from contact angle measurements	dispersive energy	$42.7 \pm 0.3$	$42.6 \pm 0.2$
	polar energy	$16.0 \pm 0.5$	$12.2 \pm 2.1$
	surface energy	$58.7 \pm 0.3$	$54.8 \pm 2.3$

<sup>a</sup>The values denoted by  $\dagger$ ,  $\ddagger$ , \$, and  $\parallel$  in the parentheses are from previous studies using NEXAFS, <sup>28</sup> electron energy loss spectroscopy (EELS), <sup>60</sup> hydrogen forward scattering (HFS), <sup>38</sup> and nano-indentation, <sup>1,43</sup> respectively. Note that the physical properties determined from Raman analysis should be interpreted as a qualitative trend only because they were derived from the empirical correlations.

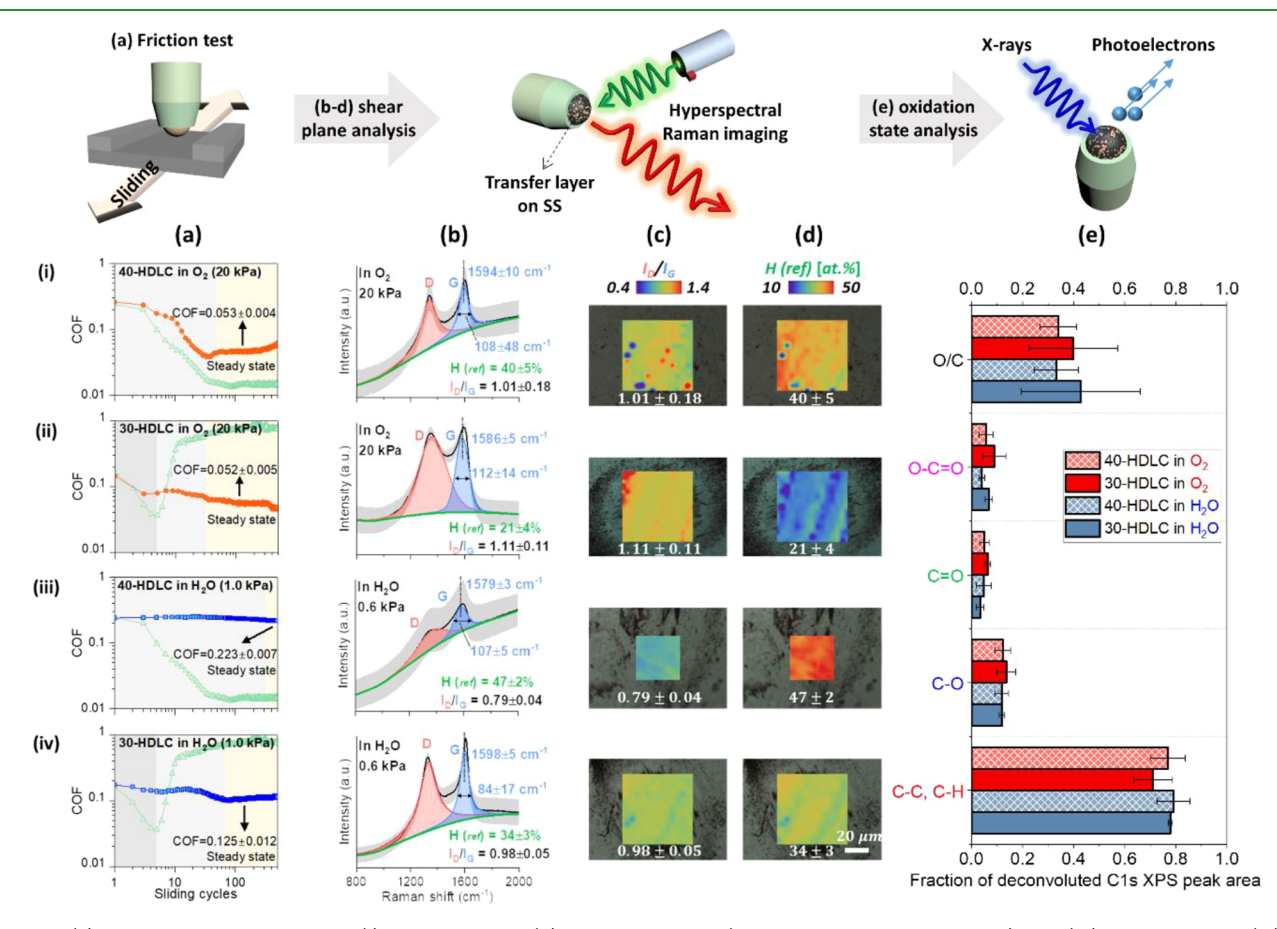


Figure 2. (a) COF measured with SS on (i) 40-HDLC and (ii) 30-HDLC in  $O_2$  (shown with an orange symbol) and (iii) 40-HDLC and (iv) 30-HDLC in  $H_2O$  (shown with a blue symbol). The COF of each HDLC measured in dry  $N_2$  is shown with green symbols as a reference in each panel (the COF data in dry  $N_2$  collected in our previous study<sup>14,25</sup>); the reproducibility of the COF data of 30-HDLC can be checked in Figures S4 and S5; the reproducibility of the COF data of 40-HDLC can be found in the previous publication.<sup>25</sup> (b) Raman spectra of the transfer layers formed on SS after sliding in  $O_2$  and  $O_2$  and  $O_3$  Raman  $O_4$  Raman H-content maps superimposed on the optical image of the transfer layers. (e) Oxidation state of the transfer layers determined with its high-resolution C 1s and O 1s XPS spectra. All quantitative values in Figure 2a,b are summarized in Table S4 in the Supporting Information. In (b), the gray-shaded regions indicate the standard deviation of the Raman spectrum calculated from the 225-pixel hyperspectral map. Optical images and histograms of the data in (c) and (d) are shown in Figure S6 in the Supporting Information.

higher oxygen content of 40-HDLC than 30-HDLC film

total surface energy was higher for the air-oxidized 40-HDLC

(Table 1). Since the dispersive component was similar, the

surface than the air-oxidized 30-HDLC surface.

3.2. Analysis of the Transfer Layer Formed in  $O_2$  and H<sub>2</sub>O Environments. Figure 2a shows how the COFs of 30and 40-HDLC films were affected by the environmental condition. Regardless of the test environment, the initial COF of 40-HDLC (0.223  $\pm$  0.007) was higher than that of 30-HDLC (0.125  $\pm$  0.012). Since both films were expected to have a similar contact area (see Section 2.2), the difference in initial COF must originate from something other than the contact size. The most likely cause would be the surface chemistry difference, i.e., a slightly higher O/C ratio of the airoxidized top surface of 40-HDLC (0.184  $\pm$  0.002) than 30-HDLC (0.144  $\pm$  0.003), which led to a slightly higher surface energy (see Table 1 and Figure S2c). After the run-in period, during which the air-oxidized films were removed by frictional shear or and shear-induced graphitization occurred, 14,18,19,32-34 40-HDLC exhibited an ultra-low COF ( $\mu \approx 0.012 \pm 0.003$ ) in dry  $N_2$ , while 30-HDLC showed a very high COF ( $\mu > 0.8$ ). The 40-HDLC surface lost this superlubricity in the presence of O<sub>2</sub> and H<sub>2</sub>O; in contrast, the presence of such gases lowered the steady-state COF of 30-HDLC (Figure 2a).

Ex situ Raman analysis of the transfer layers was conducted to obtain structural information of the shear plane. <sup>14</sup> The Raman spectra averaged over a large area of the transfer layers retrieved after the COF experiments are shown in Figure 2b, and their  $I_{\rm D}/I_{\rm G}$  and H-content maps are displayed in Figure 2c,d, respectively. In both  ${\rm O_2}$  and  ${\rm H_2O}$  environments, the degree of hydrogenation was higher for the transfer layers formed from 40-HDLC (40  $\pm$  5% after the test in  ${\rm O_2}$  and 47  $\pm$  2% after the test in  ${\rm H_2O}$ ) than those formed from 30-HDLC (21  $\pm$  4% in  ${\rm O_2}$  and 34  $\pm$  3% in  ${\rm H_2O}$ ). Note that the estimated H-content of these *oxidized* layers in  ${\rm O_2}$  and  ${\rm H_2O}$  was based on the Raman empirical correlation of pristine or *non-oxidized* HDLC films;  $^{14,56-59}$  thus, they should be taken as rough estimates, not accurate values.

Although the H-contents in the transfer layers formed from 30- and 40-HDLC in O<sub>2</sub> and H<sub>2</sub>O environments appeared quite different from each other (Figure 2b,d), all transfer layers showed a significant degree of shear-induced graphitization. Compared to the pristine film, the  $I_{\rm D}/I_{\rm G}$  ratio increased substantially, the G-band position was significantly blueshifted, and the G-band width was much narrower, which collectively indicates the occurrence of shear-induced graphitization. The G-band dispersion also showed that the sp<sup>3</sup>-C fraction in the transfer layer was quite low (<0.08; see Figure S3), confirming a high degree of sp<sup>2</sup>-C in the transfer layer. It was noted that the degree of graphitization of the transfer layer for 30- and 40-HDLC in O2 and H2O environments was quite comparable to that of the super-lubricious transfer layer formed from 40-HDLC in N<sub>2</sub> gas (green data points in panels (i) and (iii) of Figure 2a). 14 This suggested that shear-induced graphitization was not the dominant factor governing friction of HDLC; the surface chemistry of the newly exposed surface (or defect sites) during the friction test must play an important role.62

We evaluated if XPS analysis could detect any meaningful differences in chemical composition of the transfer layer. Figure 2e compares the O/C atomic ratio as well as oxygen speciation of the top  $\sim$ 10 nm region of the transfer layers formed in different conditions (two HDLCs and two environmental conditions). The O/C ratios of all transfer layers formed by friction tests in O<sub>2</sub> and H<sub>2</sub>O environments (Figure 2e) were higher than those of the air-oxidized surfaces of the pristine films ( $\sim$ 0.14 for 30-HDLC and  $\sim$ 0.18 for 40-

HDLC; Figure 1d,e). However, it could not be determined if this difference really reflects the compositional difference or is simply due to different film structures such as the size of the graphitic domain. If the film structure is different, then the degree of oxidation by air during the sample transfer from the tribo-testing cell to the XPS chamber would also be different. The variance in the O/C ratios among the transfer layers was found to be statistically insignificant (p > 0.47) in analysis of variances (ANOVA).

Combining the Raman and XPS analyses of the transfer layers, it can be concluded that both shear-induced graphitization and oxidation of the sliding interface take place in oxidizing (O<sub>2</sub> and H<sub>2</sub>O) environments. Compared to the transfer layers formed from 30- and 40-HDLC in inert (N2) or reducing (H2) environments, 14 the degree of graphitization (or graphitic nature) was found to be even larger in the oxidizing environments (Figures 2b and S3). In vacuum, dry N2, or dry H2 environments, it has been hypothesized that the degree of shear-induced graphitization of the sliding interface is a main factor governing the COF of HDLC. 14,18,32-34 However, here, the COF of 40-HDLC was significantly higher in oxidizing environments (Figure 2a) as compared to the inert and reducing environments. 14 The COF of 30-HDLC was also significantly higher in oxidizing environments (Figure 2a) as compared to the reducing H<sub>2</sub> environment,14 even though the degree of shear-induced graphitization was higher. Thus, the high friction in the oxidizing environment must have been due to the oxidation of the graphitized surface by O<sub>2</sub> and H<sub>2</sub>O molecules impinging from the gas phase.

3.3. Kinetics of Environmental Reactions. During the gas exposure between consecutive sliding cycles, the shearexposed surface was oxidized by reactions with molecules from the gas phase; the reaction products were then removed during sliding. By fitting the steady-state COF measured in various partial pressure of O<sub>2</sub> and H<sub>2</sub>O with the Langmuir-type kinetics model, the oxidation rate constant  $(k_{oxi})$  of the surface as well as the removal probability  $(\gamma)$  of reaction products by friction could be extracted.<sup>25</sup> This model assumes that the measured COF is the weighted sum of COFs of the unoxidized  $(\mu_{HDLC})$  and oxidized surfaces  $(\mu_{oxi})$  within the sliding contact region. The COFs of both conditions ( $\mu_{HDLC}$  and  $\mu_{oxi}$ ) were estimated through control experiments (see Figure S7).<sup>25</sup> Once the oxidation rate constant was obtained, the oxidation reaction probability could be estimated by simply dividing the rate constant by the partial pressure since the molecular impingement frequency is proportional to the pressure, i.e.,  $\alpha$  =  $k_{\text{oxi}}/P$ . The oxidation reaction probability in  $O_2$  ( $\alpha^{O_2}$ ) and  $H_2O$  $(\alpha^{\rm H_2O})$  is discussed in Figure 3. The removal probability  $(\gamma^{\rm O_2})$ and  $\gamma^{H_2O}$ ) is discussed in the Section 3.4.

As shown in Figure 3, the oxidation probability of 30- and 40-HDLCs in  $O_2$  and  $H_2O$  environments is on the order of  $10^{-4}-10^{-2}~\mathrm{kPa^{-1}\cdot s^{-1}}$ . These values are quite comparable magnitude-wise, to the hydrogenation reaction probability of unsaturated hydrocarbons on highly reactive noble metal catalysts such as Pt and Pd ( $\sim\!10^{-2}~\mathrm{kPa^{-1}\cdot s^{-1}}$ ).  $^{63,64}$  In both HDLC cases,  $\alpha^{\rm H_2O}$  is 3–4 times larger than  $\alpha^{\rm O_2}$ . This difference could be ascribed to the higher sticking coefficient of  $\rm H_2O$  molecules than  $\rm O_2$ .  $^{65,66}$  Unlike  $\rm O_2$ ,  $\rm H_2O$  can have hydrogen bonding interactions among physisorbed molecules and thus a longer residence time at the surface.

In Figure 3, it is also noted that the oxidation reaction probability of 30-HDLC by  $O_2$  and  $H_2O$  is significantly larger

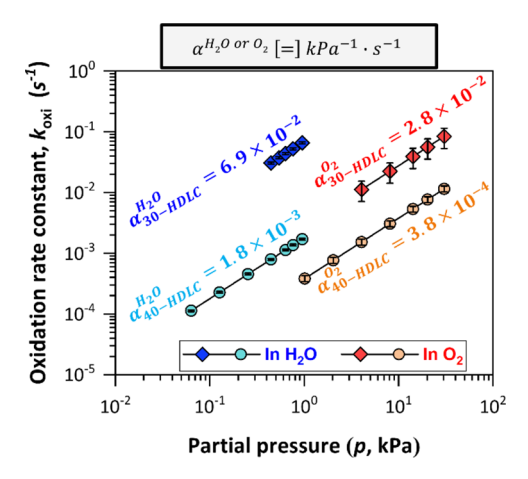


Figure 3. Oxidation rate constant of 30-HDLC and 40-HDLC as a function of partial pressure of  $\rm H_2O$  and  $\rm O_2$  ( $P_{\rm H_2O}$  and  $P_{\rm O_2}$ ) calculated by fitting the COF vs sliding cycle plot in various  $P_{\rm H_2O}$  and  $P_{\rm O_2}$  with the Langmuir-type kinetics model.  $^{25}$  The fit results of 30-HDLC can be found in Figure S5 in the Supporting Information (see our previous study  $^{25}$  for the fit results of 40-HDLC in the same gas conditions). To fit the sliding-cycle dependence of COF, the COFs of the fully oxidized ( $\mu_{\rm oxi}$ ) and unoxidized surface ( $\mu_{\rm HDLC}$ ) of 30-HDLC were determined from the control experiment described in Figure S7 in the Supporting Information (see our previous studies for  $\mu_{\rm oxi}$  and  $\mu_{\rm HDLC}$  of 40-HDLC).  $^{15,25,61}$ 

than that of 40-HDLC. The origin of this difference was investigated using reactive MD simulations of a-C with four different H-contents interacting with  $O_2$  or  $H_2O$ . The carbon atoms in the a-C that chemically reacted with O or H were tracked and used for kinetics analysis. Figure 4a,d plots the fraction of yet-to-be-reacted carbon atoms  $(\theta;\,0\leq\theta\leq1)$  as a function of time for simulations with  $O_2$  and  $H_2O$ , respectively. The fitting of this temporal change  $\left(\frac{d\theta}{dt}\right)$  required a linear combination of two exponential decay functions:

$$\frac{\mathrm{d}\theta}{\mathrm{d}t} = \theta_1 \cdot \exp(-k_1 \cdot t) + (1 - \theta_1) \cdot \exp(-k_2 \cdot t) \tag{1}$$

where  $\theta_1$  is the fraction of reactive species with the first-order rate constant  $k_1$ , and  $(1-\theta_1)$  is the fraction with  $k_2$ . The rate constants  $(k_1$  and  $k_2)$  did not vary much with H-content:  $k_1 \approx 1.3~{\rm ps}^{-1}$  in  $O_2$  and  $0.2~{\rm ps}^{-1}$  in  $H_2O$ , and  $k_2 \approx 0.012~{\rm ps}^{-1}$  in  $O_2$  and  $0.015~{\rm ps}^{-1}$  in  $H_2O$  (see Tables S1 and S2). In contrast, the fraction of highly reactive species  $(\theta_1)$  was found to decrease as the H-content increased (Figure 4c,f).

Figure 4b,e plots the total bond order (TBO) distributions of carbon atoms that reacted with O2 and H2O, respectively. In the TBO histograms, the population of TBO = 4 is zero because fully coordinated carbon atoms never react with O2 or H<sub>2</sub>O and therefore are not included in the calculation. Qualitatively, these results suggest that the relative population of extremely under-coordinated species decreases as the Hcontent in a-C:H increases, which could be correlated with the decrease in  $\theta_1$ . To show this correlation, we plotted the fraction of atoms with TBO < 3 in Figure 4c,f. Although this cutoff value for TBO is somewhat arbitrary (plots with different cutoff values are shown in Figure S10), the general trend found here is that a-C films with a higher H-content have a smaller fraction of highly reactive carbon species  $(\theta_1)$  and a lower population of extremely under-coordinated carbon species. These trends observed in reactive MD simulations

with a-C:H may explain the lower oxidation probability of 40-HDLC as compared to 30-HDLC (Figure 3).

**3.4.** Removal of Oxidation Products by Frictional Shear. In addition to the oxidation reaction probability of the surface in each environmental condition, the Langmuir-type reaction kinetics analysis of COF also provided the removal probability ( $\gamma$ ) of oxidation reaction products upon frictional shear at the steady state. Figure 5a plots the removal probability of oxidized species by friction ( $\gamma^{O_2}$  and  $\gamma^{H_2O}$ ) as a function of partial pressure of  $O_2$  and  $H_2O$  in the gas environment in which the friction test was conducted. In humid conditions, both  $\gamma^{H_2O}_{30\text{-HDLC}}$  and  $\gamma^{H_2O}_{40\text{-HDLC}}$  decreased as the partial pressure of water vapor ( $P_{H_2O}$ ) increased (i.e., as RH increased). This could be due to the lubrication effect of physisorbed water molecules.  $^{67,68}$  However, in the  $O_2$  environment,  $\gamma^{O_2}_{30\text{-HDLC}}$  and  $\gamma^{O_2}_{40\text{-HDLC}}$  exhibited opposite trends. The partial pressure dependences of  $\gamma^{H_2O}$  and  $\gamma^{O_2}$  appeared

to correlate with the wear rate of HDLC. Figure 5b plots the wear volume, normalized by the sliding distance and the applied force, of 30- and 40-HDLC films versus  $P_{O_2}$  and  $P_{H_2O_2}$ . The wear rate of 30-HDLC in dry N<sub>2</sub> was quite high because defect sites exposed by friction were not hydrogenated enough probably due to the lower H-content in the film (Figure 2a). 14 In low partial pressure of H2O, the 30-HDLC wear rate was still high, which was probably due to insufficient coverage of the physisorbed water layer. At  $P_{\rm H_2O} \approx 0.4$  kPa, where the adsorbed water forms almost complete monolayer,<sup>69</sup> the wear rate was three orders of magnitude smaller than that in low humidity conditions (RH  $\leq$  8%). Upon further increase of  $P_{\rm H_2O}$ , the wear rate of 30-HDLC continued decreasing. In the case of 40-HDLC in the RH  $\geq$  2% condition, the wear rate did not increase even though the COF was much larger than the 0% RH case. The wear rate of 40-HDLC decreased at high RH condition, which was consistent with the decrease in  $\gamma_{40\text{-HDLC}}^{n_2 \cup}$ (Figure 5a).

In the  $O_2$  environment, the 40-HDLC wear rate gradually increased as  $P_{O_2}$  increased (Figure 5b), again consistent with the  $\gamma_{40\text{-HDLC}}^{O_2}$  trend in Figure 5a. In the case of 30-HDLC, the wear rate decreased rapidly at  $P_{O_2}$  = 4.0 kPa (which is one-fifth of the atmospheric  $O_2$  concentration) and then continued decreasing as  $P_{O_2}$  increased further.

3.5. Implication to O<sub>2</sub> Partial Pressure Dependence of **HDLC Friction.** The  $\alpha^{\overline{O_2}}$  and  $\gamma^{O_2}$  obtained in this kinetics study can provide new insight into the distinct frictional behavior of 30- and 40-HDLC in oxidizing environments. Figure 6 shows the steady-state COF of 30- and 40-HDLC after the run-in period in various partial pressures of O2. The large COF difference between 30- and 40-HDLC at low  $P_{O_1}$ gradually decreased as  $P_{\mathrm{O}_2}$  increased. When  $P_{\mathrm{O}_2}$  was higher than 4.0 kPa (the yellow-shaded region), 30- and 40-HDLC had quite similar COFs at the steady state. However, the kinetics analysis with the Langmuir-type reaction model suggested a noticeable difference in the fraction of O2-oxidized components in the sliding track ( $\theta_{ss}^{O_2}$ ; see Figure S5c). Since the surface chemistry is dynamically changing during the sliding contact and between two consecutive sliding cycles, both the oxidation reaction probability ( $\alpha^{O_2}$ ; Figure 3) and the material removal probability ( $\gamma^{O_2}$ ; Figure 5a) must play important roles. The net effect of  $\alpha^{O_2}$  and  $\gamma^{O_2}$  might have resulted in convergence of the effective shear stress of 30- and

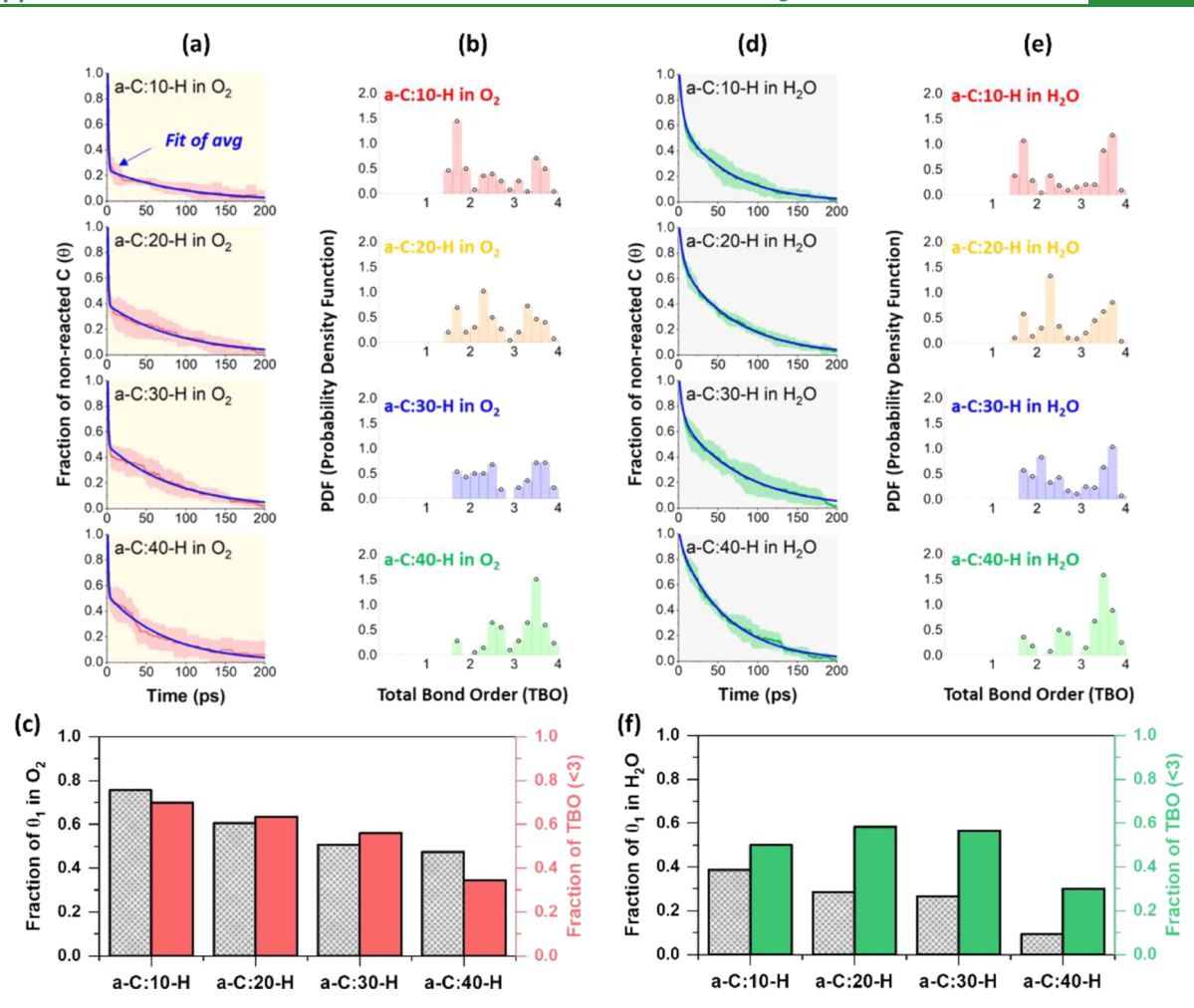


Figure 4. Simulation-calculated evolution of the fraction of yet-to-be reacted carbon atoms  $(\theta)$  of various a-C films as a function of time during reactions with (a)  $O_2$  and (d)  $H_2O$  molecules. The histogram of the total bond order (TBO) of the reacted carbon with (b)  $O_2$  and (e)  $H_2O$  molecules. Comparison of the fraction of highly reactive carbon atoms  $(\theta_1)$  to the fraction of carbon atoms with TBO < 3 of various a-C films in (c)  $O_2$  and (f)  $H_2O$  conditions. The results from individual simulations corresponding to (a) and (d) are shown in Figure S9. The relative population of TBO in (b) and (e) was depicted using the probability density function, representing the probability distribution of TBO in a histogram where the height of each histogram bar multiplied by the width of the TBO bin size is unity.

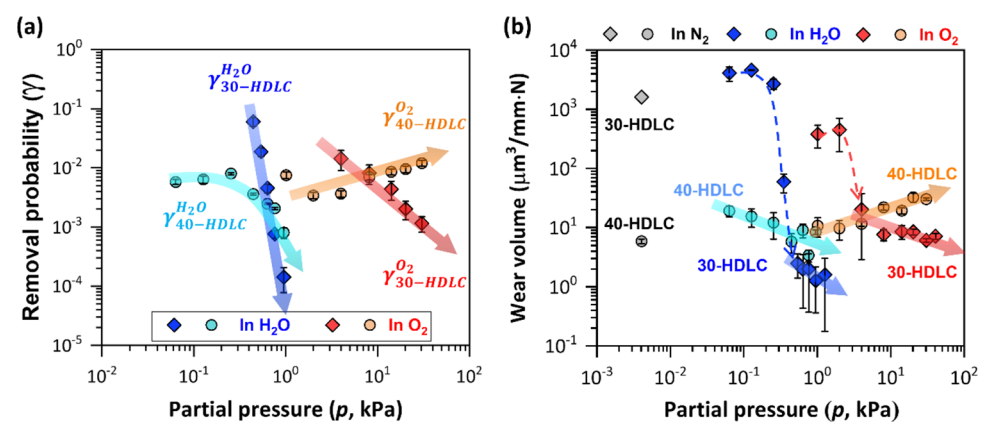
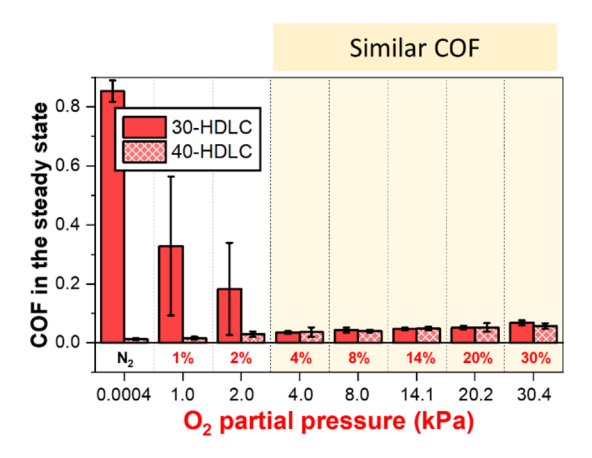


Figure 5. (a) Removal probability of re-oxidized species at the 30-HDLC and 40-HDLC surface upon frictional sliding as a function of partial pressure of  $H_2O$  and  $O_2$  ( $P_{H_2O}$  and  $P_{O_2}$ ) obtained with the Langmuir-type kinetics equation. All the data of 40-HDLC were excepted from our previous study. (b) Wear volume of 30- and 40-HDLC in dry  $N_2$  and various partial pressure of  $H_2O$  vapor and  $O_2$  gas measured with 3D optical profilometry. In  $N_2$  and low partial pressure of  $H_2O$  and  $O_2$ , 30-HDLC showed high wear. The friction data were reproducible, as can be seen in Figures S4 and S8.



**Figure 6.** COF of 30- and 40-HDLC in the steady state in various partial pressure of  $O_2$  gas. The steady-state COF values of 30-HDLC in  $P_{O_2} > 4.0$  kPa were reproducible, as shown in Figure S5 (see our previous study<sup>25</sup> for the reproducible COF data of 40-HDLC).

40-HDLC films in  $P_{\rm O_2}$  > 4.0 kPa. This argument is based on the fact that the contact areas were similar (see Section 2.2).<sup>40</sup> The individual contributions of  $\alpha^{\rm O_2}$  and  $\gamma^{\rm O_2}$  to COF could not be determined in the current study.<sup>25</sup>

**3.6.** Implications to Relative Humidity Dependence of HDLC Friction. In low humidity (RH < 14%), the steady-state COF of 30-HDLC was much larger than that of 40-HDLC (Figure 7a). This must be due to incomplete coverage of the 30-HDLC surface with water and the intrinsically high COF of 30-HDLC (see COF of 30-HDLC in dry N<sub>2</sub>; Figures

2a and S4b). In RH  $\geq$  14%, where the surface was fully covered with an adsorbed water layer<sup>69</sup> (and oxidized due to reactions with water; Figure S5c), 30-HDLC exhibited a lower COF than 40-HDLC (Figure 7a). The adsorbed water molecules can provide the vapor phase lubrication (VPL) effect; <sup>67,68</sup> if the lubrication effect of the adsorbed water layer is similar regardless of the H-content in the HDLC bulk, then the cause for this difference in COF must be something else.

In a previous study on the RH dependence of 40-HDLC, 43 it was found that the SS counter-surface undergoes galvanic corrosion when the sliding interface is transformed into the graphitic structure (so becomes electrically conductive) and the adsorbed water layer is thick enough to act like an electrolyte. Supporting this argument, Raman analysis of the transfer layers (Figure 7b,c) showed the presence of iron oxide particles such as hematite ( $Fe_2O_3$ ) and magnetite ( $Fe_3O_4$ ) at high RH conditions, which must be due to galvanic corrosion of the SS counter-surface. The presence of these particles could cause reduction of the real contact area, which may lower the sliding friction. The Raman analysis (Figure 2b) found that the degree of graphitization is larger for the 30-HDLC surface than that for the 40-HDLC. Thus, the galvanic corrosion of the SS counter-surface would occur more readily on the 30-HDLC surface. In fact, SS corrosion was evident at RH 30% for the 30-HDLC surface, while it happened at RH 40% for the 40 HDLC surface (Figure 7c). In the previous study,<sup>43</sup> when galvanic corrosion of the SS counter-surface occurred, wear of HDLC was reduced. Interestingly, the same trend was observed in this study where, at high RH, the wear of 30-

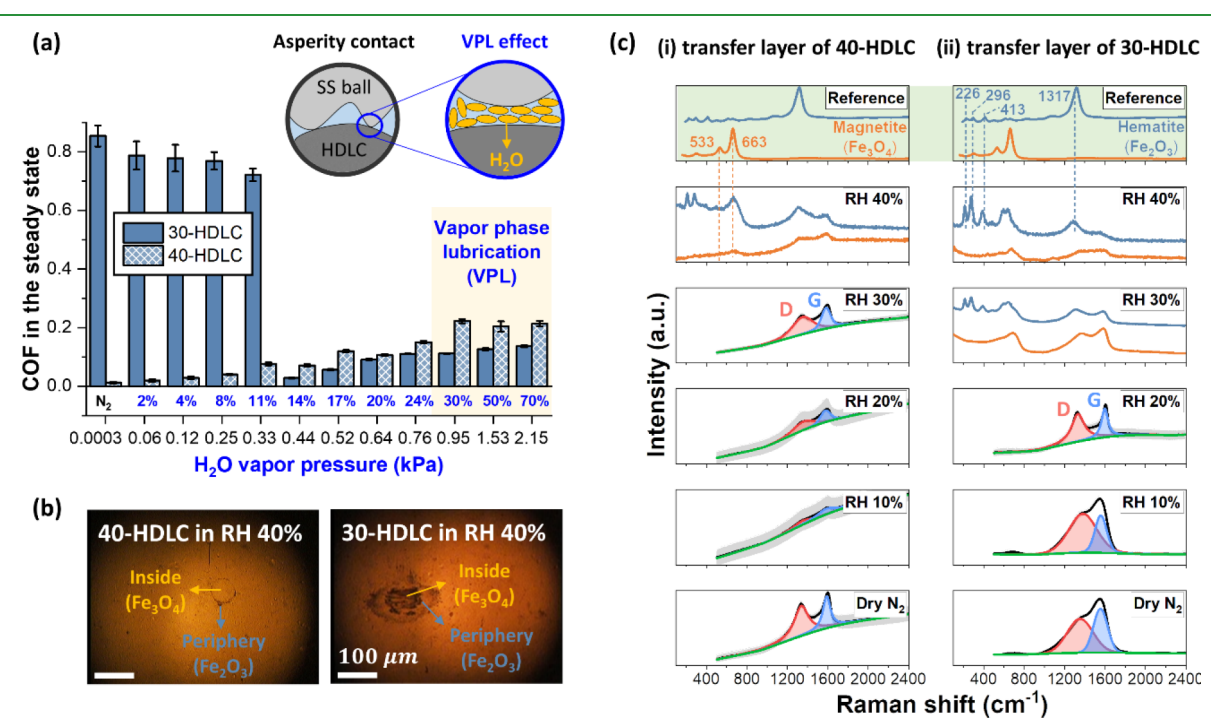


Figure 7. (a) COF of 30- and 40-HDLC at the steady state in various partial pressures of  $H_2O$  vapor. (b) Optical images of the transfer layers formed from 40-HDLC (left) and 30-HDLC (right) in RH 40%. (c) Raman spectra of the transfer layers formed from (i) 40-HDLC and (ii) 30-HDLC in dry and humid  $N_2$  conditions. In (a), the inset depicts the vapor phase lubrication induced by physisorbed water molecular layers at the sliding interface at high humidity,  $^{67,68}$  and the yellow-shaded region corresponds to the boundary lubrication regime. Reproducible COF data of 30-HDLC in (a) can be found in Figure S5 (see our previous study<sup>25</sup> for the reproducible COF data of 40-HDLC). In (c), the green-shaded panels display the Raman spectra of magnetite and hematite as a reference. Magnetite and hematite were mostly found inside and near periphery of contact area, respectively (see Figure 7b).

HDLC was found to be lower than the wear of 40-HDLC (Figure 5b).

## 4. CONCLUSIONS

The effects of the HDLC film hydrogen content and of the gas environment on the lubrication performance of HDLC were studied by analyzing the transfer layers on the counter-surface as well as partial pressure dependence of friction and wear. Raman and XPS analyses of the transfer layer suggested that the shear plane of 30- and 40-HDLC exhibits shear-induced graphitization and surface oxidation in the tested condition. From the kinetics analysis of the friction data, it was found that the oxidation probability of HDLC with O2 and H2O molecules was extremely high, comparable to that of highly reactive catalysts. The 30-HDLC surface had a higher oxidation probability than the 40-HDLC surface. Reactive MD simulations suggested that the higher oxidation probability of HDLC with a lower H-content may be due to a larger population of under-coordinated carbon species. Overall, the interplay between the oxidation and removal probability and the degree of graphitization of the shear plane were shown to be important factors governing the distinct friction and wear behaviors of HDLC in oxidizing gas environments.

## ASSOCIATED CONTENT

# Supporting Information

The Supporting Information is available free of charge at https://pubs.acs.org/doi/10.1021/acsami.3c05316.

Detailed Raman analysis, contact angle measurements, and friction tests of HDLCs and transfer layers; tabulated Raman band parameters of HDLC films and transfer layers; detailed simulation-calculated temporal change of the fraction of yet-to-be-reacted carbon atoms  $(\theta)$  of a-C:H films; and tabulated kinetic parameters of a-C:H films obtained from MD simulation (PDF)

#### AUTHOR INFORMATION

# **Corresponding Author**

Seong H. Kim — Department of Chemical Engineering and Materials Research Institute, Pennsylvania State University, University Park, Pennsylvania 16802, Unites States;
o orcid.org/0000-0002-8575-7269; Email: shk10@psu.edu

#### **Authors**

Seokhoon Jang — Department of Chemical Engineering and Materials Research Institute, Pennsylvania State University, University Park, Pennsylvania 16802, Unites States; orcid.org/0000-0002-9198-7853

Muztoba Rabbani — Department of Mechanical Engineering, University of California, Merced, California 95343, Unites States

Andrew L. Ogrinc – Department of Chemical Engineering and Materials Research Institute, Pennsylvania State University, University Park, Pennsylvania 16802, Unites States

Maxwell T. Wetherington — Materials Research Institute, Pennsylvania State University, University Park, Pennsylvania 16802, Unites States

Ashlie Martini — Department of Mechanical Engineering, University of California, Merced, California 95343, Unites States; orcid.org/0000-0003-2017-6081

Complete contact information is available at:

https://pubs.acs.org/10.1021/acsami.3c05316

#### Notes

The authors declare no competing financial interest.

## ACKNOWLEDGMENTS

This work was supported by the National Science Foundation (Grant No. CMMI-1912199, 2038494, and 2038499). The authors acknowledge Dr. Osman Levent Eryilmaz and Prof. Ali Erdemir for providing HDLC samples used in this study. All Raman, XPS, and contact angle measurements were performed in the Materials Characterization Laboratory in the Materials Research Institute at Pennsylvania State University.

## **■** REFERENCES

- (1) Jeng, Y. R.; Islam, S.; Wu, K. T.; Erdemir, A.; Eryilmaz, O. Investigation of Nano-Mechanical and- Tribological Properties of Hydrogenated Diamond Like Carbon (DLC) Coatings. *J. Mech.* **2017**, 33, 769–776.
- (2) Erdemir, A.; Donnet, C. Tribology of diamond-like carbon films: recent progress and future prospects. *J. Phys. D: Appl. Phys.* **2006**, *39*, R311.
- (3) Lipson, M.; Heald, D. A.; Sigal, I. Lithography supports with defined burltop topography. U.S. Patent 0,173,312, June 10, 2021.
- (4) Sohrabibabaheidary, D.; Mason, C. J.; Helmus, P.; Akbas, M. A.; Albert, B.; Dawson, B. D. Laser roughening: engineering the roughness of the burl top. U.S. Patent 0,134,480, May 5, 2022.
- (5) Shankar, S.; Kumar, P. K. Frictional characteristics of diamond like carbon and tungsten carbide/carbon coated high carbon high chromium steel against carbon in dry sliding conformal contact for mechanical seals. *Mech. Ind.* **2017**, *18*, 115.
- (6) Camargo, S., Jr.; Gomes, J.; Carrapichano, J.; Silva, R.; Achete, C. Silicon-incorporated diamond-like coatings for Si3N4 mechanical seals. *Thin Solid Films* **2005**, 482, 221–225.
- (7) Vanhulsel, A.; Velasco, F.; Jacobs, R.; Eersels, L.; Havermans, D.; Roberts, E.; Sherrington, I.; Anderson, M.; Gaillard, L. DLC solid lubricant coatings on ball bearings for space applications. *Tribol. Int.* **2007**, *40*, 1186–1194.
- (8) Li, X.-W.; Joe, M.-W.; Wang, A.-Y.; Lee, K.-R. Stress reduction of diamond-like carbon by Si incorporation: A molecular dynamics study. *Surf. Coat. Technol.* **2013**, 228, S190–S193.
- (9) Jungnickel, G.; Köhler, T.; Frauenheim, T.; Haase, M.; Blaudeck, P.; Stephan, U. Structure and chemical bonding in amorphous diamond. *Diamond Relat. Mater.* **1996**, *5*, 175–185.
- (10) Bustillo, K. C.; Petrich, M. A.; Reimer, J. A. Characterization of amorphous hydrogenated carbon using solid-state nuclear magnetic resonance spectroscopy. *Chem. Mater.* **1990**, *2*, 202–205.
- (11) Johnson, J. A.; Woodford, J. B.; Rajput, D.; Kolesnikov, A. I.; Schleuter, J. A.; Eryilmaz, O. L.; Erdemir, A. Carbon-hydrogen bonding in near-frictionless carbon. *Appl. Phys. Lett.* **2008**, 93, No. 131911
- (12) Erdemir, A. The role of hydrogen in tribological properties of diamond-like carbon films. *Surf. Coat. Technol.* **2001**, *146-147*, 292–297.
- (13) Erdemir, A.; Eryilmaz, O.; Nilufer, I.; Fenske, G. Synthesis of superlow-friction carbon films from highly hydrogenated methane plasmas. *Surf. Coat. Technol.* **2000**, *133-134*, 448–454.
- (14) Jang, S.; Kim, S. H. Distinct effects of endogenous hydrogen content and exogenous hydrogen supply on superlubricity of diamond-like carbon. *Carbon* **2023**, 202, 61–69.
- (15) Marino, M. J.; Hsiao, E.; Chen, Y.; Eryilmaz, O. L.; Erdemir, A.; Kim, S. H. Understanding run-in behavior of diamond-like carbon friction and preventing diamond-like carbon wear in humid air. *Langmuir* **2011**, *27*, 12702–12708.
- (16) Gao, F.; Erdemir, A.; Tysoe, W. T. The Tribological Properties of Low-friction Hydrogenated Diamond-like Carbon Measured in Ultrahigh Vacuum. *Tribol. Lett.* **2005**, *20*, 221–227.

ī

- (17) Andersson, J.; Erck, R.; Erdemir, A. Frictional behavior of diamondlike carbon films in vacuum and under varying water vapor pressure. *Surf. Coat. Technol.* **2003**, *163-164*, 535–540.
- (18) Manimunda, P.; Al-Azizi, A.; Kim, S. H.; Chromik, R. R. Shear-Induced Structural Changes and Origin of Ultralow Friction of Hydrogenated Diamond-like Carbon (DLC) in Dry Environment. *ACS Appl. Mater. Interfaces* **2017**, *9*, 16704–16714.
- (19) Sanchez-Lopez, J.; Erdemir, A.; Donnet, C.; Rojas, T. Friction-induced structural transformations of diamondlike carbon coatings under various atmospheres. *Surf. Coat. Technol.* **2003**, *163-164*, 444–450.
- (20) Eryilmaz, O. L.; Erdemir, A. Surface analytical investigation of nearly-frictionless carbon films after tests in dry and humid nitrogen. *Surf. Coat. Technol.* **2007**, *201*, 7401–7407.
- (21) Fontaine, J.; Belin, M.; Le Mogne, T.; Grill, A. How to restore superlow friction of DLC: the healing effect of hydrogen gas. *Tribol. Int.* **2004**, *37*, 869–877.
- (22) Fontaine, J.; Donnet, C.; Grill, A.; LeMogne, T. Tribochemistry between hydrogen and diamond-like carbon films. *Surf. Coat. Technol.* **2001**, *146-147*, 286–291.
- (23) Kim, H. I.; Lince, J. R.; Eryilmaz, O. L.; Erdemir, A. Environmental effects on the friction of hydrogenated DLC films. *Tribol. Lett.* **2006**, *21*, 51–56.
- (24) Li, H.; Xu, T.; Wang, C.; Chen, J.; Zhou, H.; Liu, H. Humidity dependence on the friction and wear behavior of diamond-like carbon film in air and nitrogen environments. *Diamond Relat. Mater.* **2006**, 15, 1585–1592.
- (25) Jang, S.; Chen, Z.; Kim, S. H. Environmental effects on superlubricity of hydrogenated diamond-like carbon: Understanding tribochemical kinetics in O<sub>2</sub> and H<sub>2</sub>O environments. *Appl. Surf. Sci.* **2022**, 580, No. 152299.
- (26) Li, H.; Xu, T.; Wang, C.; Chen, J.; Zhou, H.; Liu, H. Tribochemical effects on the friction and wear behaviors of a-C:H and a-C films in different environment. *Tribol. Int.* **2007**, *40*, 132–138.
- (27) Mangolini, F.; McClimon, J. B.; Rose, F.; Carpick, R. W. Accounting for nanometer-thick adventitious carbon contamination in X-ray absorption spectra of carbon-based materials. *Anal. Chem.* **2014**, *86*, 12258–12265.
- (28) Mehta, N. J.; Roy, S.; Johnson, J. A.; Woodford, J.; Zinovev, A.; Islam, Z.; Erdemir, A.; Sinha, S.; Fenske, G.; Prorok, B. X-ray studies of near-frictionless carbon films. *MRS Online Proc. Libr.* **2020**, *843*, 271–276.
- (29) Yang, M.; Marino, M. J.; Bojan, V. J.; Eryilmaz, O. L.; Erdemir, A.; Kim, S. H. Quantification of oxygenated species on a diamond-like carbon (DLC) surface. *Appl. Surf. Sci.* **2011**, *257*, 7633–7638.
- (30) Wang, K.; Zhang, J.; Ma, T.; Liu, Y.; Song, A.; Chen, X.; Hu, Y.; Carpick, R. W.; Luo, J. Unraveling the Friction Evolution Mechanism of Diamond-Like Carbon Film during Nanoscale Running-In Process toward Superlubricity. *Small* **2021**, *17*, No. 2005607.
- (31) Campbell, C. T. Transition metal oxides: extra thermodynamic stability as thin films. *Phys. Rev. Lett.* **2006**, *96*, No. 066106.
- (32) Merkle, A. P.; Erdemir, A.; Eryilmaz, O. L.; Johnson, J. A.; Marks, L. D. In situ TEM studies of tribo-induced bonding modifications in near-frictionless carbon films. *Carbon* **2010**, *48*, 587–591.
- (33) Chen, X.; Zhang, C.; Kato, T.; Yang, X.-A.; Wu, S.; Wang, R.; Nosaka, M.; Luo, J. Evolution of tribo-induced interfacial nanostructures governing superlubricity in aC: H and aC: H: Si films. *Nat. Commun.* **2017**, *8*, 1675.
- (34) Scharf, T.; Singer, I. Monitoring transfer films and friction instabilities with in situ Raman tribometry. *Tribol. Lett.* **2003**, *14*, 3–8.
- (35) Scharf, T. W.; Singer, I. L. Role of the Transfer Film on the Friction and Wear of Metal Carbide Reinforced Amorphous Carbon Coatings During Run-in. *Tribol. Lett.* **2009**, *36*, 43–53.
- (36) Wang, Z.-L. Elastic and inelastic scattering in electron diffraction and imaging; Springer Science & Business Media, 2013.
- (37) daFonseca, B. G.; Thind, S. S.; Brolo, A. G. Raman maps reveal heterogeneous hydrogenation on carbon materials. *J. Raman Spectrosc.* **2021**, *52*, 516–524.

- (38) Johnson, J. A.; Woodford, J. B.; Chen, X.; Andersson, J.; Erdemir, A.; Fenske, G. R. Insights into "near-frictionless carbon films.". J. Appl. Phys. 2004, 95, 7765–7771.
- (39) Popov, V. L. Contact mechanics and friction; Springer, 2010.
- (40) He, X.; Liu, Z.; Ripley, L. B.; Swensen, V. L.; Griffin-Wiesner, I. J.; Gulner, B. R.; McAndrews, G. R.; Wieser, R. J.; Borovsky, B. P.; Wang, Q. J.; Kim, S. H. Empirical relationship between interfacial shear stress and contact pressure in micro- and macro-scale friction. *Tribol. Int.* **2021**, *155*, No. 106780.
- (41) Amontons, G. De la Resistance Cause'e dans les Machines. J. Jpn. Soc. Tribol. 1999, 44, 229–235.
- (42) Barthel, A. J.; Luo, J.; Hwang, K. S.; Lee, J.-Y.; Kim, S. H. Boundary lubrication effect of organic residue left on surface after evaporation of organic cleaning solvent. *Wear* **2016**, *350-351*, 21–26.
- (43) Alazizi, A.; Draskovics, A.; Ramirez, G.; Erdemir, A.; Kim, S. H. Tribochemistry of Carbon Films in Oxygen and Humid Environments: Oxidative Wear and Galvanic Corrosion. *Langmuir* **2016**, *32*, 1996–2004.
- (44) Liu, S. B.; Peyronnel, A.; Wang, Q. J.; Keer, L. M. An extension of the Hertz theory for three-dimensional coated bodies. *Tribol. Lett.* **2005**, *18*, 303–314.
- (45) Thomson, G. W. The Antoine equation for vapor-pressure data. *Chem. Rev.* **1946**, 38, 1–39.
- (46) Ferrari, A. C.; Robertson, J. Interpretation of Raman spectra of disordered and amorphous carbon. *Phys. Rev. B* **2000**, *61*, 14095.
- (47) Cui, W.; Lai, Q.; Zhang, L.; Wang, F. Quantitative measurements of sp<sup>3</sup> content in DLC films with Raman spectroscopy. *Surf. Coat. Technol.* **2010**, 205, 1995–1999.
- (48) Zhang, L.; Wei, X.; Lin, Y.; Wang, F. A ternary phase diagram for amorphous carbon. *Carbon* **2015**, *94*, 202–213.
- (49) Lajaunie, L.; Pardanaud, C.; Martin, C.; Puech, P.; Hu, C.; Biggs, M.; Arenal, R. Advanced spectroscopic analyses on a: CH materials: Revisiting the EELS characterization and its coupling with multi-wavelength Raman spectroscopy. *Carbon* **2017**, *112*, 149–161.
- (50) Merlen, A.; Buijnsters, J.; Pardanaud, C. A Guide to and Review of the Use of Multiwavelength Raman Spectroscopy for Characterizing Defective Aromatic Carbon Solids: from Graphene to Amorphous Carbons. *Coatings* **2017**, *7*, 153.
- (51) Fowkes, F. M. Quantitative characterization of the acid-base properties of solvents, polymers, and inorganic surfaces. *J. Adhes. Sci. Technol.* **1990**, *4*, 669–691.
- (52) Plimpton, S. Fast parallel algorithms for short-range molecular dynamics. *J. Comput. Phys.* **1995**, *117*, 1–19.
- (53) Stukowski, A. Visualization and analysis of atomistic simulation data with OVITO—the Open Visualization Tool. *Modell. Simul. Mater. Sci. Eng.* **2009**, *18*, No. 015012.
- (54) Wang, Y.; Su, Y.; Zhang, J.; Chen, Q.; Xu, J.; Bai, S.; Ootani, Y.; Ozawa, N.; De Barros Bouchet, M.-I.; Martin, J. M. Reactive molecular dynamics simulations of wear and tribochemical reactions of diamond like carbon interfaces with nanoscale asperities under H2 gas: Implications for solid lubricant coatings. *ACS Appl. Nano Mater.* 2020, 3, 7297–7304.
- (55) Ferrari, A.; Robertson, J.; Benedek, G.; Milani, P.; Ralchenko, V. Nanostructured carbon for advanced applications. *J. Nano Car. Adv. Appl.* **2001**, 24, 177.
- (56) Casiraghi, C.; Piazza, F.; Ferrari, A. C.; Grambole, D.; Robertson, J. Bonding in hydrogenated diamond-like carbon by Raman spectroscopy. *Diamond Relat. Mater.* **2005**, *14*, 1098–1102.
- (57) Casiraghi, C.; Ferrari, A.; Robertson, J. Raman spectroscopy of hydrogenated amorphous carbons. *Phys. Rev. B* **2005**, *72*, No. 085401.
- (58) Marchon, B.; Gui, J.; Grannen, K.; Rauch, G. C.; Ager, J. W.; Silva, S.; Robertson, J. Photoluminescence and Raman spectroscopy in hydrogenated carbon films. *IEEE Trans. Magn.* **1997**, 33, 3148–3150.
- (59) Rose, F.; Wang, N.; Smith, R.; Xiao, Q.-F.; Inaba, H.; Matsumura, T.; Saito, Y.; Matsumoto, H.; Dai, Q.; Marchon, B.; Mangolini, F.; Carpick, R. W. Complete characterization by Raman spectroscopy of the structural properties of thin hydrogenated

- diamond-like carbon films exposed to rapid thermal annealing. *J. Appl. Phys.* **2014**, *116*, No. 123516.
- (60) Ponsonnet, L.; Donnet, C.; Varlot, K.; Martin, J.; Grill, A.; Patel, V. EELS analysis of hydrogenated diamond-like carbon films. *Thin Solid Films* **1998**, 319, 97–100.
- (61) Al-Azizi, A. A.; Eryilmaz, O.; Erdemir, A.; Kim, S. H. Surface structure of hydrogenated diamond-like carbon: origin of run-in behavior prior to superlubricious interfacial shear. *Langmuir* **2015**, *31*, 1711–1721.
- (62) Chen, Z.; Khajeh, A.; Martini, A.; Kim, S. H. Chemical and physical origins of friction on surfaces with atomic steps. *Sci. Adv.* **2019**, *5*, No. eaaw0513.
- (63) Yoshida, H.; Koizumi, K.; Boero, M.; Ehara, M.; Misumi, S.; Matsumoto, A.; Kuzuhara, Y.; Sato, T.; Ohyama, J.; Machida, M. High Turnover Frequency CO–NO Reactions over Rh Overlayer Catalysts: A Comparative Study Using Rh Nanoparticles. *J. Phys. Chem. C* 2019, 123, 6080–6089.
- (64) Panagiotopoulou, P. Hydrogenation of CO<sub>2</sub> over supported noble metal catalysts. *Appl. Catal., A* **2017**, *542*, 63–70.
- (65) Böttcher, A.; Niehus, H. Oxygen adsorbed on oxidized Ru (0001). *Phys. Rev. B* **1999**, *60*, 14396.
- (66) Carosella, C.; Comas, J. Oxygen sticking coefficients on clean (111) silicon surfaces. Surf. Sci. 1969, 15, 303–312.
- (67) Briscoe, W. H.; Titmuss, S.; Tiberg, F.; Thomas, R. K.; McGillivray, D. J.; Klein, J. Boundary lubrication under water. *Nature* **2006**, 444, 191–194.
- (68) Barthel, A. J.; Kim, S. H. Lubrication by physisorbed molecules in equilibrium with vapor at ambient condition: effects of molecular structure and substrate chemistry. *Langmuir* **2014**, *30*, 6469–6478.
- (69) Alazizi, A.; Smith, D.; Erdemir, A.; Kim, S. H. Silane Treatment of Diamond-Like Carbon: Improvement of Hydrophobicity, Oleophobicity, and Humidity Tolerance of Friction. *Tribol. Lett.* **2016**, *63*, 1–11.